Geophysical Journal International

Geophys. J. Int. (2023) **234,** 2520–2534
Advance Access publication 2023 June 27
GJI Seismology

https://doi.org/10.1093/gji/ggad257

Moment magnitude for earthquakes in the Etna volcano area

Angela Saraò [1], Luca Moratto [1], Elisabetta Giampiccolo [2] and Ornella Cocina [2]

[1] *Istituto Nazionale di Oceanografia e di Geofisica Sperimentale – OGS, Trieste I*34010*, Italy. E-mail: asarao@ogs.it*
[2] *Istituto Nazionale di Geofisica e Vulcanologia – Sezione di Catania, Osservatorio Etneo,* 95125*, Italy*

Accepted 2023 June 21. Received 2023 May 5; in original form 2023 February 6

SUMMARY

Accurate quantification of seismic activity in volcanic regions is an important asset for improving hazard and risk assessment. This is especially true for densely populated areas, as in the case of Etna volcano (Southern Italy). There, the volcanic hazard is amplified by the seismic risk of active faults, especially on the eastern flank of the volcano. In such a context, it is common to rely on moment magnitude (M_W) to characterize seismicity and monitor the energy released during an eruption. In this study, we calculate the moment-based magnitude (M_W) for selected seismic data sets, using different approaches in distinct magnitude ranges to cover the widest possible range of magnitude that characterizes Etna's seismicity. Specifically, we computed the M_W from a data set of moment tensor solutions of earthquakes that occurred in the magnitude range $3.4 \leq M_L \leq 4.8$ during 2005–2020; we created a data set of seismic moment and associated M_W for earthquakes $1.0 \leq M_L < 3.4$ obtained by analysing source spectra; we fine-tuned two relationships, for shallow and deep earthquakes, to obtain M_W from response spectra. Finally, we calibrated a specific relationship between M_W and M_L for the Etna area earthquakes in the range $1.0 \leq M_L \leq 4.8$. All the empirical relationships obtained in this study can be applied in real-time analysis of the seismicity to provide fast and robust information on the released seismic energy.

Key words: Earthquake source observations; Volcano seismology; Waveform inversion; Time series analysis; Earthquake hazards; Moment magnitude; Full moment tensor; Response spectra.

1 INTRODUCTION

Quantifying the seismic moment in volcanic areas is important for understanding volcanic dynamics and is particularly important in densely populated areas where volcanic and seismic hazards are combined. The seismic moment can be used to estimate the volume of intruded magma and thus the probability of an impending eruption and to monitor energy status during an eruption (e.g. Bonaccorso & Giampiccolo 2020; Meyer *et al.* 2021); furthermore, the magnitude scale based on seismic moment is a crucial parameter for seismic hazard assessment.

The moment magnitude (M_W, Kanamori 1983) is the most widely used magnitude scale for tectonophysical and seismological applications, and it is routinely calculated using relationships based on seismic moment (Hanks & Kanamori 1979). In the point-source approximation, the seismic moment (M_0), which represents the size of an earthquake in terms of the dislocation phenomenon, can be estimated by computing the solutions of the moment tensor (Julian *et al.* 1998, and reference therein) or from source spectra corrected for path propagation and possible site effects (e.g. Andrews 1986; Ottemöller & Havskov 2003; Atkinson *et al.* 2014; Moratto *et al.* 2019; Eulenfeld *et al.* 2021).

Compared to the traditional local magnitude (M_L, Richter 1935), which refers to the peak amplitude and is determined by relatively high frequencies, M_W is unsaturated. Moreover, it is obtained from signals with very low frequencies and is therefore less affected by attenuation or amplification effects.

It has become a common practice to convert M_L to equivalent M_W values. However, M_L–M_W relationships depend on various parameters such as stiffness, rupture velocity, attenuation and stress drop (Kanamori *et al.* 1993; Bormann & Di Giacomo 2015). The empirical relationships used in bulletins and catalogues may not be comparable between different regions (Gasperini *et al.* 2012) and while in many cases, differences may be negligible compared to the uncertainty in magnitude determination, in volcanic areas magnitude values are severely biased when a magnitude scale from another area is used (Havskov *et al.* 2003). Therefore, it is advisable to estimate M_W from M_0 unless the conversion equation has been reliably determined using local grid data (e.g. Edwards & Douglas 2014).

Specially calibrated relationships have been published for Hawaii, Vesuvius, Deception Island, Etna and Campi Flegrei (Zúñiga *et al.* 1988; Del Pezzo & Petrosino 2001; Havskov *et al.* 2003; Giampiccolo *et al.* 2007; Petrosino *et al.* 2008; Guardato *et al.* 2022). In this study, we aim to calculate the M_W for Etna seismicity using the most suitable approaches to cover the characteristic magnitude range of Etna seismicity.

Etna, an active stratovolcano on the east coast of Sicily (Italy), is an area of high seismic hazard (Azzaro *et al.* 2015). The tectonic features of Etna are commonly interpreted as the result of the interaction of regional tectonic and local volcanic processes. Volcanic activity is characterized by persistent activity from summit craters with episodic paroxysmal events and flank eruptions that are usually preceded and accompanied by strong seismic swarms of volcano-tectonic (VT) earthquakes (Patanè *et al.* 2004, and reference therein). Seismicity rarely exceeds M_L 4 and usually consists of frequent weak VT events (local magnitude $M_L < 3$) with a hypocentral depth of less than 5 km, mainly affecting the eastern flank of the volcano where there is morphological evidence of active faults (Azzaro *et al.* 2012; Fig. 1). The southern and eastern flanks are the most tectonically active areas of the volcano and have been the site of the strongest earthquakes in the last two centuries (D'Amico *et al.* 2016), causing severe damage and even destruction. The largest damaging earthquakes in the Etna area (e.g. 1633 M_W 4.8 Nicolosi; 1669 M_W 4.8 Nicolosi; 1818 M_W 6.2 Aci Catena; 1914 I = IX–X, Linera) have been documented by historical research (Rovida *et al.* 2020, 2022) and are well described in Azzaro & D'Amico (2019). The recent larger earthquakes (1984 M_L 4.4 Fleri; 2002 M_L 4.5 S. Venerina; and 2018 M_W 4.9 Fleri), due to the activation of the Timpe Fault System (TFS in Fig. 1) on the eastern flank, occurred in the higher urban areas of the Etna region and had a significant impact on the seismic hazard (Villani *et al.* 2020).

Several authors (Patanè *et al.* 1994, 1995, 1997; Centamore *et al.* 1997) computed the source spectra parameters of weak earthquakes of Mt. Etna and found empirical relationships M_L - M_0 and M_L - M_W in the past. However, a suitable attenuation model for the local upper crust had not been adequately explored at that time. New relationships were proposed by Giampiccolo *et al.* (2007), who used a large data set of local earthquakes and detailed and robust information on seismic attenuation at depths less than 5 km. Analyses were also performed to estimate the seismic moment tensor of low-magnitude seismicity before the eruption 1991–1993 (Saraò *et al.* 2001) and the 2001 (Saraò *et al.* 2010). After feasibility tests to tune the algorithm and evaluate the sensitivity of the solutions to the velocity model and station geometry, Saraò *et al.* (2001, 2010) used short-period seismograms to compute moment tensor solutions for 28 earthquakes ($2.0 \leq M_D \leq 3.0$) that occurred from 1990 August to 1991 December (Saraò *et al.* 2001) and a sample of 61 earthquakes ($2.0 \leq M_D \leq 3.8$) that occurred in the early hours of a seismic swarm leading up to the 2001 July eruption (Saraò *et al.* 2010). In addition to the seismic moment and the focal mechanism, the authors observed an increasing trend of the non-double-couple components of the studied earthquakes immediately preceding the two eruptions, possibly due to the response of the confining rocks to the rising magma and to degassing processes, as well as to the complex interaction between tectonic stress and volcanic activity.

Following the development of the broadband seismic network managed by INGV-Osservatorio Etneo (INGV-OE), and in order to obtain a near real-time estimate of the full moment tensor, a new analysis of 50 earthquakes with $M_W \geq 3.4$ occurred during the period 2005–2013 was performed, which allowed obtaining a preliminary M_L–M_W relationship (Saraò *et al.* 2016). To obtain this relationship on a larger data sample and also to extend the magnitude range investigated, the 2005–2013 moment tensor solutions were merged with the moment tensor solutions from Saraò *et al.* (2010), obtaining a data set with 111 solutions for the magnitude range $2.0 \leq M_L \leq 4.7$. For the 2001 data, only M_D was available, and M_L was derived by the empirical relation M_L–M_D of Tuvè *et al.* (2015).

In this study, we update the moment tensor solutions obtained by Saraò *et al.* (2016) and extend the data set with new moment tensor solutions of earthquakes that occurred in the magnitude range $3.4 \leq M_L \leq 4.8$ in the 2005–2020 period and provide a dense data set of seismic moment and associated M_W for earthquakes $1.0 \leq M_L < 3.4$ obtained by analysing source spectra. Also, we fine-tune a relationship for the Etna region to obtain M_W from response spectra (Atkinson *et al.* 2014; Moratto *et al.* 2017). After describing the data analysis and results, we merge all calculated M_W estimates using moment tensor and spectra analysis. Finally, we calibrate a specific relationship between M_W and M_L for the Etna area earthquakes.

2 THE COMPLETE SEISMIC MOMENT TENSOR ANALYSIS

We compute the full seismic moment tensor for the highest energy VT earthquakes ($3.4 \leq M_L \leq 4.8$) using the full-time domain moment tensor technique (Dreger 2003; Minson & Dreger 2008). The minimum magnitude of earthquakes that we can process with this method is about 3.5, because of limits imposed by background noise in the frequency passband (Dreger *et al.* 1998). However, we begin processing events with $M_L \geq 3.4$ to account for possible variations in the determination of M_L. We selected 71 earthquakes with $M_L \geq 3.4$ recorded by the INGV-OE broadband (0.01–40 s) seismic network during 2005–2020 (Table 1) among those with a signal-to-noise ratio (SNR) greater than 5 (Fig. 1, blue circles). The seismic waveforms of the three components were inverted after removing the instrumental response in the frequency range of 0.02–0.10 or 0.02–0.05 Hz. The Green's functions used in the inversion were computed as synthetic displacement seismograms using a frequency–wavenumber integration method (Saikia 1994) for a homogeneous stratified velocity structure (Alparone *et al.* 2012; Martinez-Arevalo *et al.* 2005) called 'Etna' for our convenience. The fit between observed and synthetic seismograms was quantified by the variance reduction (VR), which is equal to the sum of the squares of the amplitude difference normalized by the observed waveforms Therefore, VR is the quality parameter of inversion results (100 per cent is best) considered acceptable with VR $\geq$ 50. Source depth was determined iteratively by finding the solution that maximizes VR. The full solution of the moment tensor provides the orientation parameters (strike, dip and rake) of the two nodal planes, the scalar seismic moment and the percentage of the double couple (DC) and non-double couple, that is represented by the compensated linear vector dipole (CLVD) and volumetric (ISO) part. The size of the ISO, CLVD and DC is evaluated in per cent using the following formulae:

$$\mathrm{DC} = \left(1 - 2\frac{M^*_{|\min|}}{M^*_{|\max|}}\right) * 100 * c \quad \mathrm{CLVD} = 2\frac{M^*_{|\min|}}{M^*_{|\max|}} * 100 * c \quad \mathrm{ISO} = \frac{1}{3}\frac{Tr\,(M)}{M_{|\max|}} * 100 * c; \tag{1}$$

where Tr(**M**) is the trace of the seismic moment tensor **M,** $M_{|\max|}$ is the absolute maximum eigenvalue of **M**, $M^*_{|\max|}$ and $M^*_{|\min|}$ are

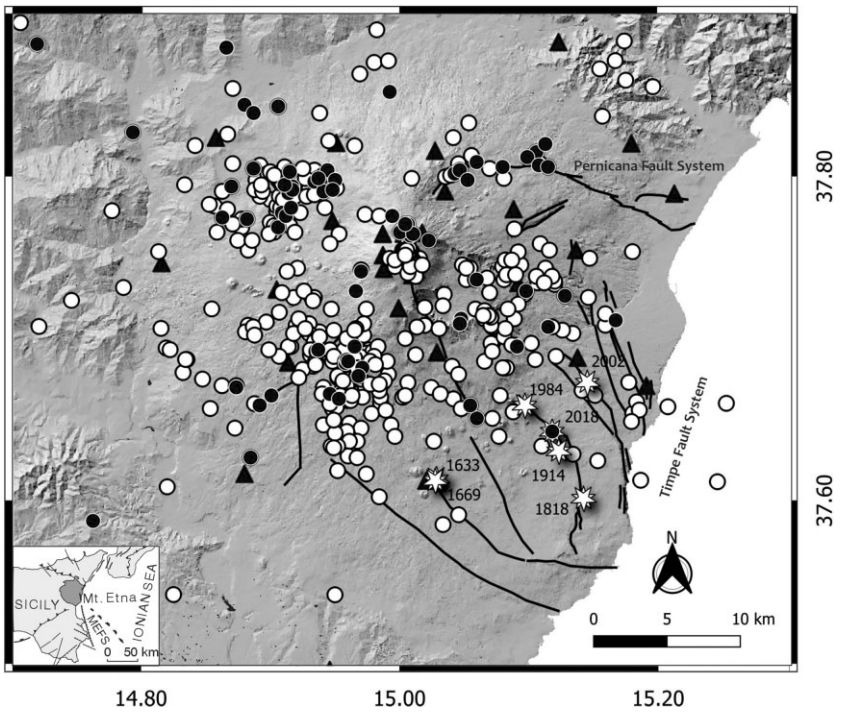

Figure 1. Digital Elevation Map with the main tectonic elements, the TFS and the PFS and the permanent broad-band seismic stations (black triangles) of the INGV-OE network. The black and white circles are the earthquakes used for the moment tensor and spectral analysis, respectively. The white stars indicate the macroseismic location of some destructive earthquakes in the Etna area (Rovida *et al.* 2020, 2022). The inset map shows the location of the Etna volcano and the main regional fault systems, including the Malta Escarpment Fault System (MEFS).

the maximum and minimum absolute eigenvalues of the deviatoric moment tensor and $c = (1 + \mathrm{Tr(M)}/3\mathrm{M}_{|\max|})$.

Sensitivity tests (e.g.; Dreger & Helmberger 1993; Dreger *et al.* 1998; Saraò *et al.* 2021) have shown that long-period body waves within the frequency band of 0.02–0.10 Hz, are relatively insensitive to lateral mislocations, and that models representative of the coarse changes in crustal thickness, average crustal velocity and near-surface velocity can provide robust estimates of the source parameters with a limited number of stations, although the source depth parameter may be unstable. To verify the robustness of the solutions, we performed some tests using two different starting models, the 'Etna' (Fig. 2a) and the 'Sicily' (Fig. 2b) models. 'Etna' model was obtained by velocity and attenuation tomography of local earthquakes at Etna (Alparone *et al.* 2012); 'Sicily' model by active and passive tomography for eastern Sicily, including the Peloritan-Southern Calabria region and the volcanic environment of Etna and the Aeolian Islands (Dìaz Moreno *et al.* 2018).

An example is shown in Figs 3(a) and (b), where the same event (no. 61 in Table 1) was studied using the 'Etna' and 'Sicily' models.

The best solution obtained with the 'Sicily' model shows the same orientation of the fault plane with a difference of 0.1 for M_W and 2 km for depth; the CLVD value is greater than that of the 'Etna' model, as a spurious effect of the inversion obtained by using a velocity model not specifically retrieved for the study area (Panza & Saraò 2000).

The moment tensor solutions obtained within this study are reported in Table 1 and Fig. 4. The first 50 solutions are an update of the solutions reported in Saraò *et al.* (2016), the last 21 solutions are new. For some events, it was possible to compare the solutions with INGV-TDMT (Scognamiglio *et al.* 2006) and RCMT (Pondrelli 2002), that use different velocity models, different data, different algorithms and invert in diverse frequency bands. Although the fault plane solutions generally agree well (Cocina *et al.* 2020), we found differences in the M_W up to ± 0.2 for a few events. Saraò *et al.* (2016) reported a similar error for the 2005–2013 moment tensor solutions of seismicity, therefore, to be conservative, we adopted ± 0.2 as the maximum error for our M_W estimates. For the aim of this study, we also considered the M_w values of the inversions with VR < 50 when independent estimates of M_W were compatible with our estimates within the uncertainty interval.

The orientation of the best DC solutions obtained by computing the full moment tensor (Fig. 4), mainly NNW-SSE and NE-SW, are consistent with the structural environment of the Etna area showing the coexistence of different types of source mechanisms, with a prevalence of strike-slip motions with subordinate dip-slip components, both normal and reverse (e.g. Patanè & Giampiccolo 2004). The complete solutions of the moment tensor also provide useful information as an indicator of local changes in the stress field caused by dyke injection, high fluid pressure, or thermal cooling; the earthquake source can be investigated by the seismic moment tensor, which is decomposed into DC—linked to shear displacements—CLVD—which may be due to lenticular crack activation associated with possible fluid motion—and the ISO part—which represents volume changes (e.g. Julian *et al.* 1998). Nevertheless, it is well known that the possible distortion effects of wave propagation in structurally complicated regions, the presence of noise, or inappropriate station coverage can make the identification of non-DC as true source phenomena uncertain (e.g. Julian *et al.* 1998), and feasibility tests can be helpful in interpreting results in the context of physical processes at the source (e.g. Panza & Saraò 2000; Rösler and Stein 2022). In our analysis, we selected the solutions that minimize the non-DC components, and we list the percentage of DC, CLVD and ISO components for each event (Table 1).

Table 1. Earthquakes investigated in this study by moment tensor. For each event are reported: progressive number (N), date (Date), time (Time UTC), Latitude N (Lat), Longitude E (Long) in degrees, M_L, depth in km (Dep), Variance Reduction (VR), strike (Str1), dip (Dip1), rake (Rak1), percentage of DC, CLVD, ISO, M_W and M_0.

N	Date	Time	Lat (°)	Long (°)	Ml	Dep (km)	VR	Str1 (°)	Dip1 (°)	Rak1 (°)	DC (per cent)	CLVD (per cent)	ISO (per cent)	M_W	M_0 10e+21 (dyne cm)
1	2005-07-10	13:38:51	37.852	14.991	3.4	29	45.3	189	79	−36	38	39	23	3.4	1.34E + 00
2	2005-08-14	21:56:48	37.815	15.104	3.5	2	69.7	20	87	144	38	13	49	3.7	3.40E + 00
3	2005-10-30	06.06:50	37.652	15.058	3.7	9	68	47	74	23	14	53	33	3.8	6.22E + 00
4	2005-10-31	00:02:41	37.66	15.053	3.8	4	71.1	64	63	46	79	15	6	3.9	6.03E + 00
5	2006-01-08	16:09:24	37.683	14.97	3.7	12	70.4	178	87	−142	75	12	13	3.8	6.34E + 00
6	2006-03-02	20:35:38	37.794	14.916	3.4	20	43	195	78	36	24	35	41	3.2	7.48E + 00
7	2006-05-20	07:05:56	37.667	14.945	3.8	10	60.2	87	68	27	27	26	47	3.7	4.21E + 00
8	2006-06-19	20:55:34	37.844	14.879	4.0	24	68	102	64	−145	71	24	5	4	8.48E + 00
9	2006-06-20	13:16:35	37.839	14.886	3.4	24	20	127	63	−122	49	8	44	3.3	9.90E - 01
10	2006-12-19	14:58:05	37.775	14.862	4.5	26	64	102	89	−174	50	37	13	4	1.15E + 01
11	2006-12-20	01:46:23	37.778	14.908	3.4	24	42.7	209	71	21	48	19	32	3.7	3.95E + 00
12	2008-04-09	04:14:36	37.727	15.126	3.5	8	86.4	108	81	34	59	25	16	3.8	6.49E + 00
13	2008-05-01	21:05:47	37.802	15.041	3.5	1	66.3	80	85	−29	29	33	38	3.7	3.82E + 00
14	2008-05-13	09:23:04	37.776	14.993	3.6	6	64.6	232	78	−155	43	42	16	3.7	4.01E + 00
15	2008-05-13	09:28:05	37.764	15.007	3.8	2	67.1	193	64	−39	58	25	17	3.8	5.10E + 00
16	2008-05-13	09:56:38	37.761	15.021	3.6	5	60.1	81	85	−59	73	16	11	3.7	3.37E + 00
17	2008-05-13	10:07:48	37.771	15.005	3.9	2	67.6	142	60	−141	84	14	2	3.7	4.61E + 00
18	2008-05-13	11:03:32	37.768	15.001	3.7	6	63.1	273	88	159	14	35	50	3.5	1.81E + 00
19	2008-05-13	11:52:38	37.766	14.999	3.6	2	63.2	248	54	−84	22	38	40	3.5	1.69E + 00
20	2008-05-13	12:13:42	37.765	15.009	3.8	1	45.9	164	62	109	12	85	3	3.9	7.03E + 00
21	2008-05-13	13:26:49	37.771	15.003	3.7	2	58.8	234	77	32	70	24	7	3.7	4.38E + 00
22	2008-05-13	21:28:27	37.809	15.058	3.4	1	75.5	179	88	−174	15	33	52	3.6	2.75E + 00
23	2008-12-16	02:30:14	37.664	14.952	4.0	8	68.2	162	70	−157	91	5	4	3.7	3.35E + 00
24	2009-03-14	09:26:51	37.73	15.096	3.5	6	75.3	36	90	−176	45	49	6	3.5	2.18E + 00
25	2009-05-13	14:13:46	37.712	15.165	3.6	2	68.6	220	82	−17	40	10	51	3.9	8.26E + 00
26	2009-07-23	00:10:42	37.589	14.763	3.7	22	52.8	263	80	−13	17	62	21	3.6	3.26E + 00
27	2009-08-25	16:58:02	37.812	15.097	3.6	2	70.9	274	80	−29	7	72	21	3.6	2.43E + 00
28	2009-12-19	05:36:00	37.79	14.913	4.4	22	51	205	57	64	47	18	35	4.5	7.39E + 01
29	2009-12-19	07:42:25	37.774	14.881	3.7	22	69.7	203	64	69	43	49	8	3.9	8.10E + 00
30	2009-12-19	08:01:10	37.769	14.905	3.6	20	50.8	239	56	122	55	1	44	3.8	6.61E + 00
31	2009-12-19	08:24:57	37.776	14.911	3.8	19	62.7	223	63	95	57	15	28	4.1	1.43E + 01
32	2009-12-19	09:01:14	37.794	14.869	4.8	28	56.4	217	65	64	87	6	6	4.7	1.32E + 02
33	2009-12-19	12:35:40	37.781	14.915	3.5	20	61.7	15	88	−55	30	26	45	3.6	3.33E + 00
34	2009-12-19	12:43:10	37.792	14.916	3.8	24	64.5	269	84	156	58	24	18	3.9	7.51E + 00
35	2009-12-19	18:08:33	37.805	14.886	3.5	20	27	186	59	−139	71	3	26	3.5	1.92E + 00
36	2009-12-23	14:24:42	37.795	14.91	3.7	18	54.5	255	58	106	24	40	36	3.7	3.36E + 00
37	2010-04-02	20:04:00	37.806	15.078	4.3	3	65.1	8	79	163	59	9	32	4.3	2.67E + 01
38	2010-04-02	20:21:55	37.807	15.106	3.5	2	56.7	99	81	13	23	69	9	3.4	1.35E + 00
39	2011-05-06	15:12:35	37.804	14.943	4.0	14	92.4	274	72	129	44	52	4	4	1.17E + 01
40	2011-05-06	15:15:23	37.798	14.949	3.4	23	22.5	269	83	164	81	14	5	3.4	1.56E + 00
41	2011-05-06	15:18:30	37.803	14.914	3.4	20	17.6	282	89	166	14	6	80	3.4	1.55E + 00
42	2011-05-06	19:28:49	37.797	14.933	3.5	20	56.1	352	76	17	87	8	4	3.5	2.05E + 00
43	2011-09-09	22:23:44	37.827	14.793	4.0	26	64.2	239	84	102	55	43	2	3.9	6.95E + 00
44	2012-01-01	04:17:02	37.879	14.865	3.5	32	32.2	107	83	163	74	23	4	3.8	5.03E + 00
45	2012-11-22	09:10:41	37.791	14.94	4.2	12	84.3	262	71	159	95	5	0	3.9	7.02E + 00
46	2012-11-22	11:25:51	37.799	14.936	4.3	20	72.1	253	70	125	64	6	29	4.2	1.98E + 01
47	2012-11-22	11:28:55	37.792	14.947	3.9	12	91.2	262	76	155	82	10	8	3.8	6.50E + 00
48	2013-01-04	07:50:06	37.881	14.719	4.4	12	65.5	79	58	−137	52	25	23	4.2	2.20E + 01
49	2013-05-23	13:04:48	37.696	15.089	4.0	3	30.7	142	89	18	32	50	18	3.4	1.34E + 00
50	2015-04-20	01:07:42	37.806	15.113	3.6	2	63.3	360	58	137	83	17	0	3.4	1.30E + 00
51	2015-12-08	09:28:29	37.804	15.045	3.6	2	52.7	175	88	−168	14	81	6	3.7	4.30E + 00
52	2017-01-30	09:51:07	37.678	14.967	3.6	12	64.3	91	88	−54	78	13	8	3.8	5.50E + 00
53	2018-06-02	07:40:54	37.708	15.113	3.4	8	53.5	242	78	162	56	22	22	3.4	1.70E + 00
54	2018-07-18	21:20:36	37.73	14.965	3.6	5	30.2	218	83	−138	59	33	7	3.5	2.70E + 00
55	2018-10-06	00:34:19	37.628	14.884	4.7	10	70.8	352	88	169	97	3	0	4.6	9.30E + 01
56	2018-11-20	05:06:34	37.666	14.9	3.5	10	14.6	48	74	−161	27	64	9	3.5	2.30E + 00
57	2018-12-24	10:27:01	37.82	15.111	3.5	4	37.4	293	70	40	75	16	9	3.5	2.40E + 00
58	2018-12-24	11:01:50	37.742	14.969	4.0	1	53.3	23	81	−169	57	29	14	3.9	8.40E + 00
59	2018-12-24	12:08:56	37.713	15.046	4.0	1	54.3	177	77	−34	71	17	11	3.9	7.30E + 00
60	2018-12-24	16:50:10	37.71	15.045	4.3	1	80.8	74	87	−167	77	23	0	4.3	3.80E + 01
61	2018-12-24	19:26:19	37.686	14.957	4.0	2	63.5	348	77	166	81	16	3	3.9	7.30E + 00
62	2018-12-25	12:45:43	37.66	14.891	3.5	10	50	94	80	−18	52	47	1	3.8	5.70E + 01

Table 1. Continued

N	Date	Time	Lat (°)	Long (°)	Ml	Dep (km)	VR	Str1 (°)	Dip1 (°)	Rak1 (°)	DC (per cent)	CLVD (per cent)	ISO (per cent)	M_W	M_0 10e+21 (dyne cm)
63	2018-12-26	02:19:14	37.644	15.116	4.8	2	69.4	40	88	−15	75	8	17	4.9	2.80E + 02
64	2019-01-04	04:10:36	37.694	14.936	3.5	1	25.6	96	48	27	74	15	12	3.6	2.90E + 00
65	2019-01-08	23:50:34	37.798	15.051	4.1	2	50.4	252	66	−29	79	11	10	4.0	1.30E + 01
66	2019-07-08	04:38:28	37.671	14.873	3.8	22	54.5	262	69	54	56	38	6	3.9	7.80E + 00
67	2019-12-17	23:48:43	37.843	14.905	3.8	16	19.2	209	81	37	81	15	4	3.5	2.00E + 00
68	2020-03-22	10:32:12	37.737	15.058	3.4	7	22.7	220	72	−157	66	23	11	3.6	3.80E + 00
69	2020-12-31	20:30:52	37.688	14.958	3.5	8	55.4	75	90	−32	43	48	9	3.5	2.40E + 00
70	2020-12-31	20:58:10	37.687	14.959	3.4	8	43	255	85	27	45	32	23	3.5	2.10E + 00
71	2020-12-31	21:54:39	37.696	14.964	3.7	6	62.6	260	89	33	59	39	2	3.7	3.80E + 00

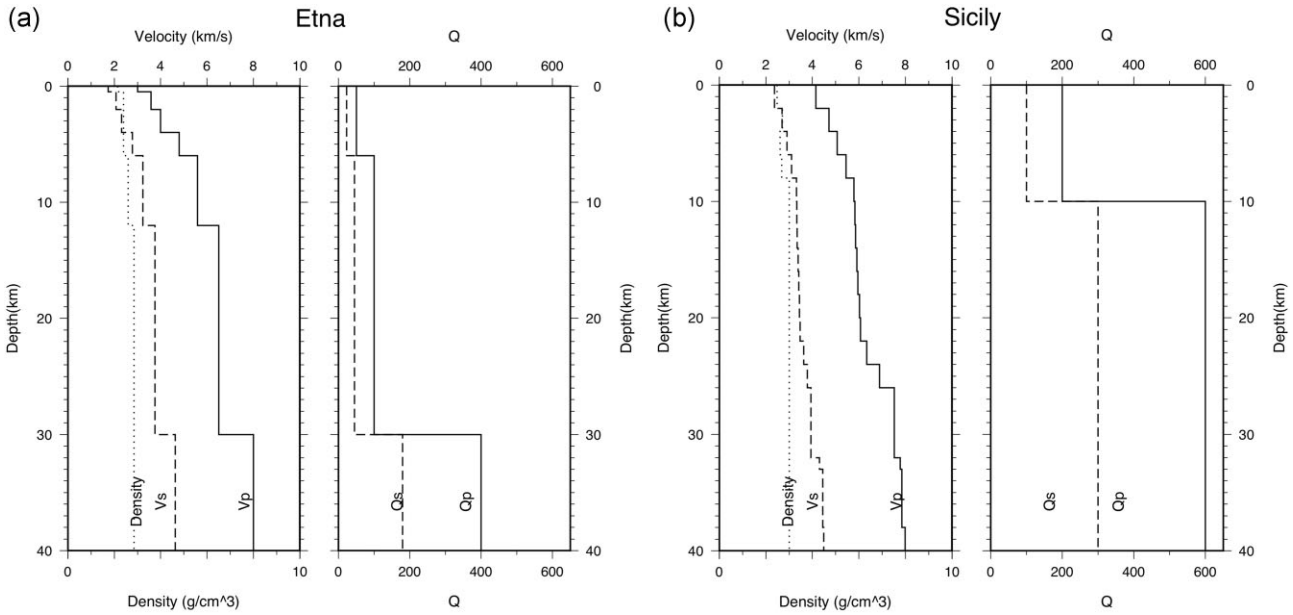

Figure 2. (a) Velocity and attenuation model named 'Etna' used in the waveform inversions for the moment tensor computation. (b) Velocity model named 'Sicily' was used in the preliminary testing phase.

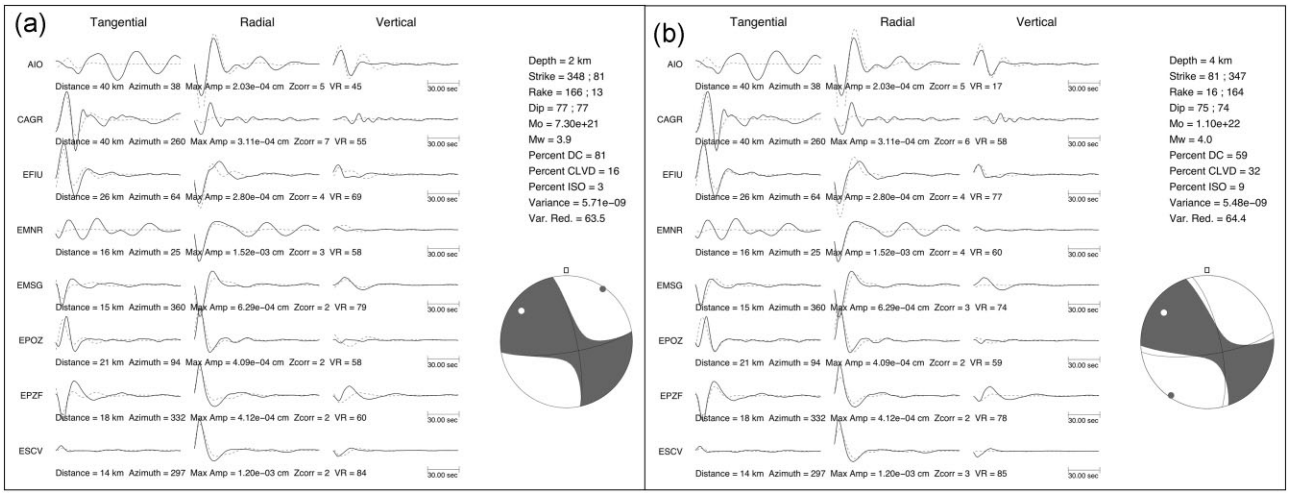

Figure 3. Example of waveform inversions: (a) event no. 61 (Table 1) studied using the velocity model 'Etna'; and (b) event no. 61 (Table 1) studied using the velocity model 'Sicily'.

Interpreting the percentage of DC or non-DC components for each earthquake requires investigation and analysis beyond the scope of this paper, so we limit ourselves to some speculative considerations of the overall results. In Fig. 5(a), we plot all the solutions obtained for the study period, while in Fig. 5(b), we show only the solutions for the events that occurred in the area of the Pernicana Fault System (PFS, Fig. 1). DC dominates throughout the study area, probably due to the activation of regional tectonic

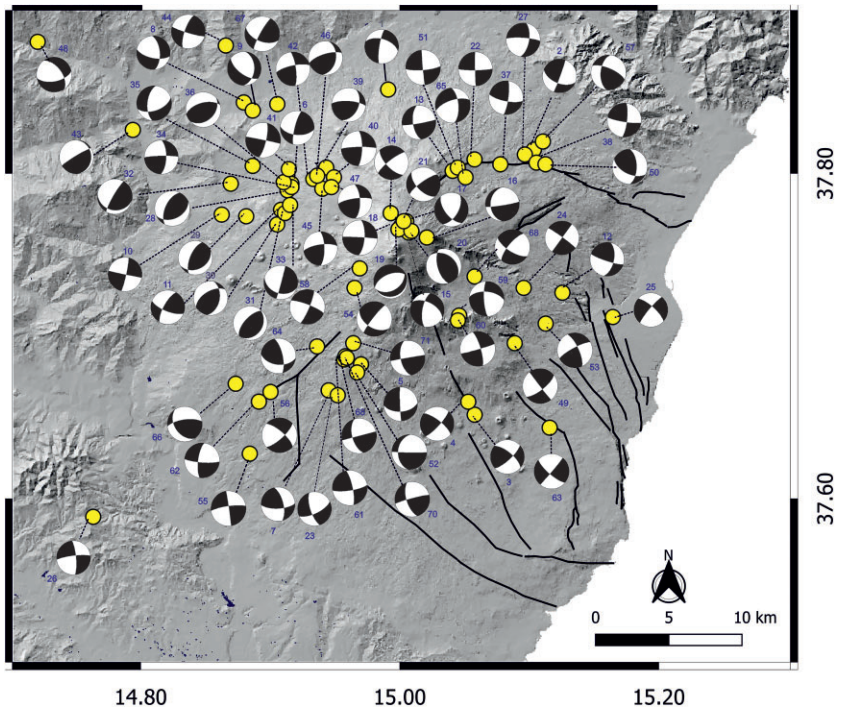

Figure 4. Etna Digital Elevation Map reporting the epicentres (circles) and the 71 best DC solutions (beach balls) of the earthquakes investigated in this study.

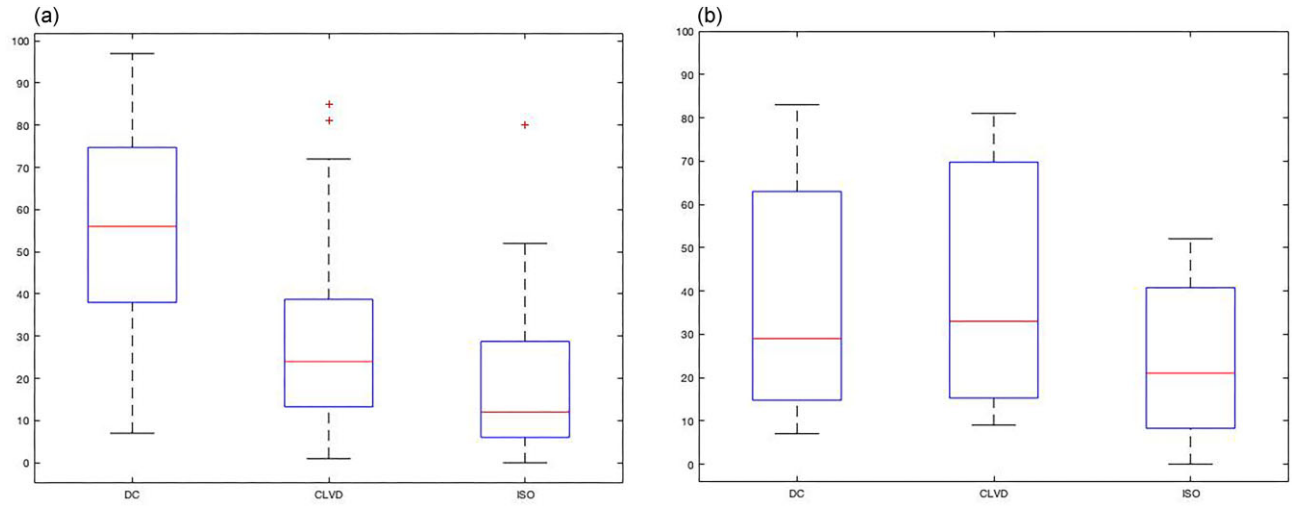

Figure 5. Boxplots showing the percentage of the components of the moment sensor (DC, CLVD and ISO) for the overall area (a) and the Pernicana fault area (b). On each box, the central mark is the median, the edges of the box are the 25th and 75th percentiles, the whiskers extend to the most extreme data points not considered outliers.

structures and the formation of the dry eruptive field during the 2008 Etna eruption (e.g. Alparone *et al.* 2012; Azzaro *et al*. 2020), while the solutions in the Pernicana fault area are predominantly not DC, as would be expected in an area where fluid circulation has been observed by geophysical and geochemical measurements (Siniscalchi *et al.* 2010).

3 SEISMIC MOMENT FROM RESPONSE SPECTRA

3.1 Method

To obtain an independent estimate of M_W for the magnitude events $M_L < 3.4$, we used the method of Atkinson *et al.* (2014), already applied in other areas (e.g. Moratto *et al.* 2017; Lanzoni *et al.* 2020), that calculates M_0 from response spectra computed at various periods. The approach uses response spectra calculated at selected periods (0.3 and 1.0 s) that intercept the plateau of the source spectra, and it is effective for $M_W < 4$ to avoid any finite-fault effects (Atkinson *et al.* 2014). Response spectra computed at 1.0 s are on the flat low frequency of a standard Brune (1970) point-source displacement spectrum over a wide range of stress-drop values; for smaller events (e.g. $M_W < 3$ in Atkinson *et al.* 2014), the contribution of noise at 1.0 s can be relevant and lead to an overestimation of magnitude, so response spectra computed at 0.3 s perform better.

The advantage of using response spectra instead of Fourier amplitude spectra is that they are computed using 5 per cent damping and

smooth out the irregularities observed in Fourier spectra (Atkinson *et al.* 2014). In addition, response spectra at 0.3 and 1.0 s are widely used engineering parameters that are often available in real-time (e.g. ShakeMap parameters) and therefore can be used for rapid estimation of M_W.

Following Moratto *et al.* (2017), we consider the response spectra in terms of spectral acceleration (SA) and calibrate the following empirical function to obtain M_W values from SAs:

$$\log (SA)_T = a M_W - g(R) - b_T R + c_T \quad (2)$$

where T is the period (0.3 s or 1.0 s), R is the hypocentral distance, a is the scaling magnitude parameter, $g(R)$ is the geometrical spreading, b_T is related to anelastic attenuation and c_T is a constant defined separately for response spectra at 0.3 and 1.0 s (SA03 and SA10, respectively). Following Atkinson *et al.* (2014), the tuning of (1) can be divided into two stages: (I) a is determined by stochastic simulations (Boore 1983, 2003) and (II) b_T and c_T are calibrated by independent estimates of M_W.

For each event, the M_W value is calculated as the mean of the M_W values calculated at each station with the associated standard deviations. We used the vertical components to reduce the local soil and near-surface amplifications that mainly affect the horizontal components in volcanic environments (Bianco *et al.* 1999).

3.2 Calibration from simulated response spectra

To determine the value of a in eq. (2), we compute the synthetic seismograms using a stochastic approach (Boore 1983, 2003) for a point source model of Brune, from which we computed SA10 and SA03. The simulations are computed at a maximum distance range of 200 km for M_W ranging from 0.0 to 4.0 at 0.2 units interval, using as input the parameters proposed by Langer *et al.* (2016), who computed ground motion scenarios for Etna that distinguish between two seismotectonic regimes. One set of input parameters for shallow VT events with a focal depth of less than 5 km (typically between 1 and 2 km) is mainly associated with deformation processes at the surface affecting the volcanic edifice; the other set of parameters for earthquakes with a focal depth of more than 5 km (typically 10 km or deeper) occurs in the crystalline basement of the area and is associated with the regional pattern of crustal deformation (Langer *et al.* 2016). The selected parameters are listed in Table 2.

The magnitude scaling factor, represented by the parameter in eq. (2), ranges from 1.1 for $M_W > 2.0$ to 1.5 for $M_W \leq 1.0$, in agreement with the observations of Lanzoni *et al.* (2020). Our data set has a magnitude between 2.0 and 4.0, so we set 1.15 for surface events and 1.20 for deep events, respectively.

Trends in the corresponding SA03 and SA10 values as a function of hypocentral distance (Fig. 6) show that the SA03 data (Fig. 6a) are saturated for shallow events with $M_W > 3.0$. SA03 values are generally less sensitive to noise, and a good quality station can record an earthquake of $M_W = 1.0$ at a hypocentral distance of 50 km for deep earthquakes (Fig. 6b), while good quality records seem to be difficult for lower magnitude events. On the other hand, SA10 is not saturated at larger magnitudes but is strongly affected by noise at $M_W < 2.0$ (Figs 6c and d).

3.3 Calibration from M_W estimates of real data

To calibrate b_T and c_T, our method requires a set of M_W values that are estimated independently. For this purpose, we used a data-set of M_W derived from spectral analysis of P waves from a subset of about 400 earthquakes with $M_L \geq 1.0$ (Fig. 1), totaling about 6400 waveforms recorded by the seismic network INGV-OE since 2005. Selected data from the instrumental seismic catalogue INGV-OE (Alparone *et al.* 2015; Alparone *et al.* 2020a,b,c; Barberi *et al.* 2020; Alparone *et al.* 2022) were examined to eliminate spurious transients and double events. Only data with an SNR greater than 1.3 in the 1–25 Hz frequency band were included in the analysis. The SNR threshold was established based on previous analyses of Etna seismicity (e.g. De Gori *et al.* 2011; Alparone *et al.* 2012) and is the best compromise that does not limit the number of data and still provides robust spectral estimates. To account for the smoothing of the spectrum by a Hanning window, the window length was increased by 5 per cent. Spectra at each station were corrected for instrumental response and geometrical spreading. Spectral ratios were calculated using the average of the stations. Spectral analysis was performed with a window of 1.28 s and a sampling rate of 100 Hz to avoid contamination by the S phase. Following Scherbaum (1990), the far-field velocity spectrum $V(f)$ can be expressed as follows:

$$V(f) = 2\pi f \Omega_0 \frac{f_c^2}{(f_c^2 + f^2)} \exp(-\pi f t^*) \quad (3)$$

where Ω_0 is the low-frequency spectral level of the ground displacement spectrum proportional to the seismic moment, f_C is the cut-off frequency and $t*$ is the global absorption factor quantifying the attenuation along a ray path evaluated by fitting the amplitude spectrum decay (Eberhart-Phillips & Chadwick 2002).

Assuming the spectral model of Brune (1970) for a point source and a frequency-independent attenuation within the investigated frequency band, we estimated the corner frequency of the event using a grid search over the frequency range 1–15 Hz, which corresponds to the range of f_C usually observed for seismicity at Etna (e.g. Patanè *et al.* 1997; Patanè & Giampiccolo 2004; Giampiccolo *et al.* 2007) and all records for each event (Scherbaum 1990; Eberhart-Phillips & Chadwick 2002). The initial attenuation parameter Q was set with an average $Q = 100$ (Patanè *et al.* 1997; De Gori *et al.* 2005; Giampiccolo *et al.* 2007; De Lorenzo *et al.* 2010; De Gori *et al.* 2011). Then, for each spectrum, an iterative procedure is applied to adjust the spectral level, Ω_0, and t^*. The corner frequency common to all stations that recorded the event is fixed, which provides a more stable solution for the simultaneous inversion of all spectral parameters (see De Gori *et al.* 2005 for details). The quality of the final fit is estimated by the root mean square (RMS) between the observed and calculated spectra. The fit is discarded if RMS is equal to or greater than 0.4. The spectral parameters obtained were then used to calculate the seismic moment M_0 (Keilis-Borok 1959):

$$M_0 = 4\pi\rho v^3 R \frac{\Omega_0}{F U_{\phi,\varphi}} \quad (4)$$

where ρ is the density of the medium, R is the hypocentral distance, v is the body-waves velocity, F is the free surface factor and $U_{\varphi,\phi}$ is the mean radiation pattern. We considered V_P computed as a function of the focal depths, $\rho = 2700$ kg m^{-3}, $F = 2$ and $U\varphi$, $\phi = 0.4$ (Giampiccolo *et al.* 2007).While M_0 is usually accurately estimated from earthquake source spectra, other source parameters (e.g. corner frequency and stress drop) often exhibit considerable variability, making it difficult to constrain the dynamic properties of the source of weak events (e.g. Abercrombie 2015), in part because of the effect of near-surface attenuation, particularly in the volcanic domain (Havskov *et al.* 2003). Following Madariaga (1976), we also calculated the source radius and stress drop (Table S1 of the

Table 2. Input parameters utilized for the stochastic simulations (from Langer *et al.* 2016).

	Stress drop (bar)	$Q(f)$	$g(R)$	Bs (km s^{-1})	F_{max} (Hz)	Part. factor	Rad. pattern
Shallow events ($h < 5$ km)	5	$90*f^{0.5}$	R^{-1} $R < 40$ km $R^{-0.4}$ $R > 40$ km	1.8	5	0.707	0.63
Deep events ($h \geq 5$ km)	30	$90*f^{0.5}$	R^{-1} $R < 40$ km $R^{-0.4}$ $R > 40$ km	3.0	15	0.707	0.63

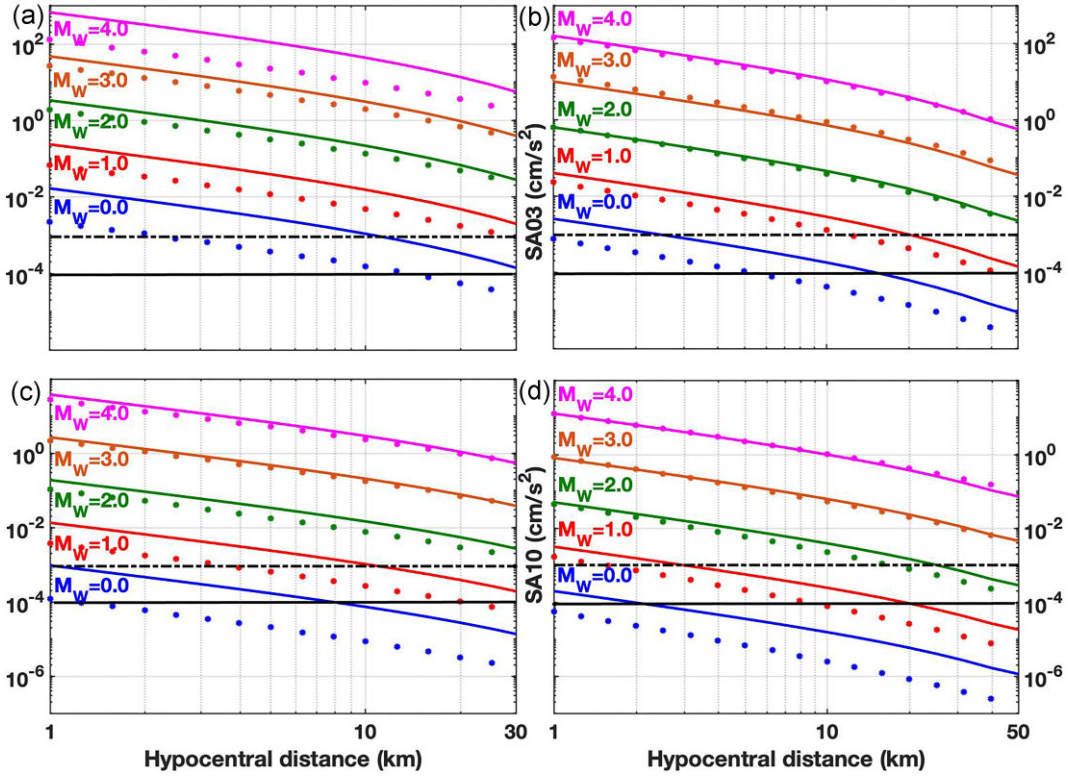

Figure 6. Simulated SA amplitudes (dots) for (a) and (c) shallow and (b) and (d) deep events along with the function that we have defined as a basis for the magnitude estimation (solid lines). The low (10^{-4} cm/ s^2) and high (10^{-3} cm/s ^{2}) noise levels (horizontal solid and dashed lines) were also drawn (Atkinson *et al.* 2014).

Supporting Information). The source radii range from about 70 to about 900 m, while the stress drops are limited between 0.01 MPa and about 60 MPa. These values are fully compatible with those obtained in previous studies for Etna seismicity in the same magnitude range (Patanè *et al.* 1997; Patanè & Giampiccolo 2004; Giampiccolo *et al.* 2007; de Lorenzo *et al.* 2010), confirming the validity of our approach.

The M_0 values calculated with relation (3) were converted to M_W (Hanks & Kanamori 1979). We refer to these values of M_W as M_W(CAL). Calibration events are uniformly distributed in the range $2.0 \leq M_W$ (CAL) ≤ 4.0 (Fig. 7); the hypocentral distance of the shallow data set (Table S2 of the Supporting Information; 98 earthquakes, 1661 vertical waveforms) is limited to 30 km (Fig. 7a). For the deep data set (Table S3 of the Supporting Information; 267 earthquakes, 3969 vertical waveforms), the hypocentral distance is limited to 50 km to limit the complexity of the propagation effects (Fig. 7b).

To fine-tune eq. (2), we calculate the SA03 and SA10 values for shallow and deep calibration earthquakes. We set the threshold for the change in magnitude estimate from M_W (SA03) to M_W (SA10) to 2.4, that is, the magnitude value at which noise can become dominant for SA10 (Fig. 6d) and bias the final results.

Thus, the M_W versus (SA) equations for shallow events are:

$$M_W\,(\mathrm{SA}) = (\log 10\,(\mathrm{SA10}) + 3.21 - g\,(R) + 0.024 * R)\,/1.15 \quad \text{for } 2.4 \leq M_W \leq 4.0 \tag{5a}$$

$$M_W\,(\mathrm{SA}) = (\log 10\,(\mathrm{SA03}) + 1.58 - g\,(R) + 0.047 * R)\,/1.15 \quad \text{for } 2.0 \leq M_W < 2.4 \tag{5b}$$

while for deep earthquakes we obtain:

$$M_W\,(\mathrm{SA}) = (\log 10\,(\mathrm{SA10}) + 3.01 - g\,(R) + 0.026 * R)\,/1.20 \quad \text{for } 2.4 \leq M_W \leq 4.0 \tag{6a}$$

$$M_W\,(\mathrm{SA}) = (\log 10\,(\mathrm{SA03}) + 1.76 - g\,(R) + 0.053 * R)\,/1.20 \quad \text{for } 2.0 \leq M_W < 2.4 \tag{6b}$$

where R is the hypocentral distance and $g(R)$ is defined as in Table 2.

These relationships reproduce the values of M_W(CAL) (Figs 8a and b) in the range $2.0 \leq M_W \leq 4.0$: the regression between M_W(CAL) and M_W(SA) was calculated using orthogonal regression (Castellaro *et al.* 2006), resulting in a scaling factor of 1.04 ± 0.27 and 1.05 ± 0.17 for shallow (Fig. 8a) and deep (Fig. 8b) events, respectively. The residuals of M_W, that is, the differences between

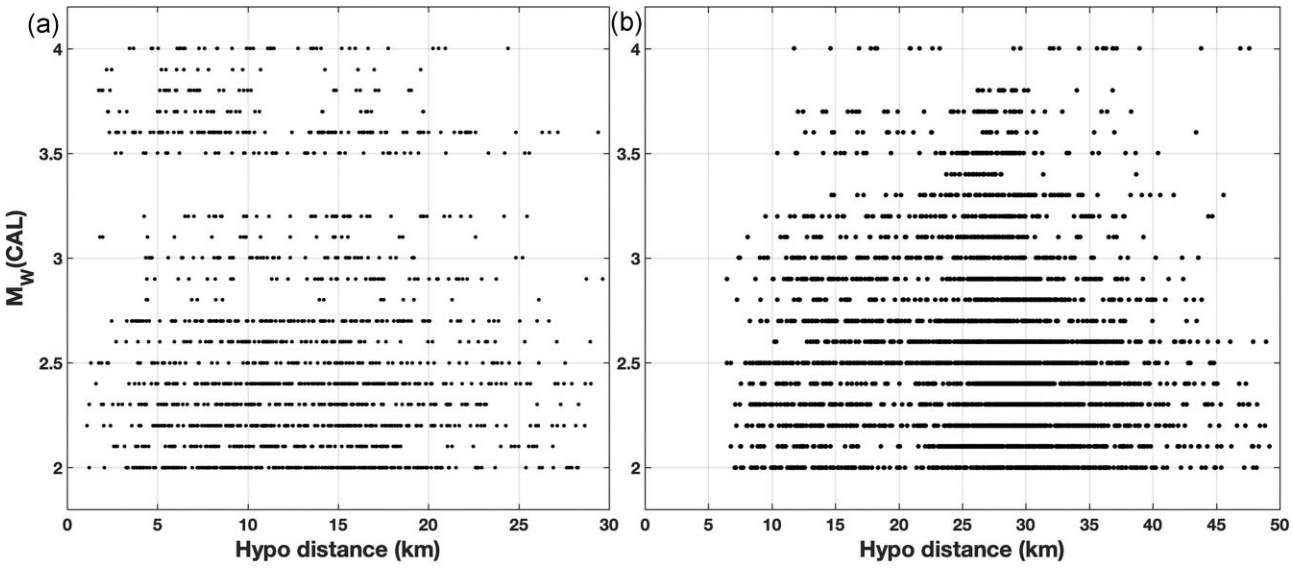

Figure 7. M_W(CAL) data set of (a) shallow and (b) deep events mapped in Fig. 1 that were used to calibrate M_W (SA) equations. For each M_W(CAL), the circles represent the available records as a function of the hypocentral distance.

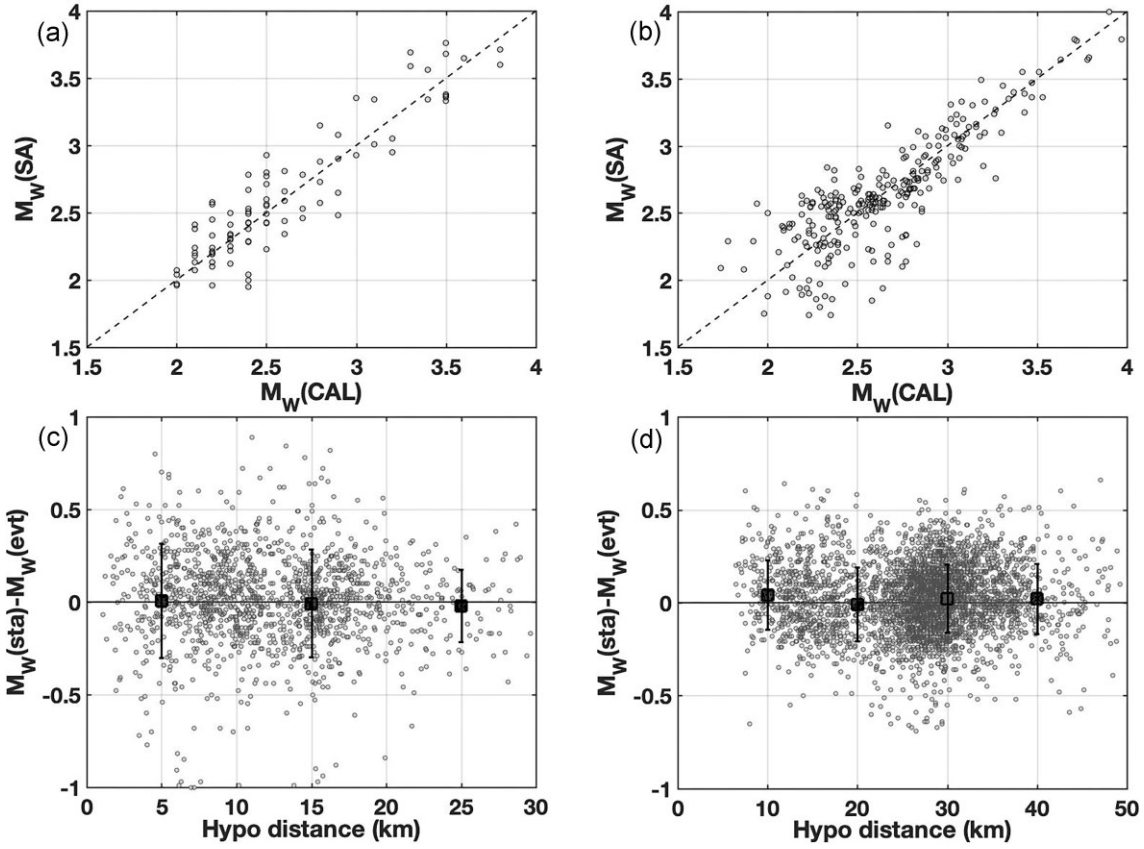

Figure 8. Comparison between magnitude computed by M_W(CAL) and M_W(SA) for (a) shallow and (b) deep events. Residuals as a function of the hypocentral distance computed for each record utilized in the calibration for (c) shallow and (d) deep earthquakes; the black bars represent the mean of the residuals calculated within equal hypocentral distances of 10 km.

the M_W calculated at each station for a single event and the average magnitude of the same earthquake, are plotted as a function of the hypocentral distance and show a homogeneous distribution around 0.5 (Figs 8c and d); no trend or bias associated with hypocentral distance is observed. Shallow events at stations close to the source show a large scatter, likely due to major hypocentral uncertainties or finite-fault effects not accounted for in our model.

The relations M_W(SA)-SA adequately reproduce the distance attenuation trend observed in the recorded data for shallow (Figs 9a–f) and deep events (Figs 9g–l) respectively.

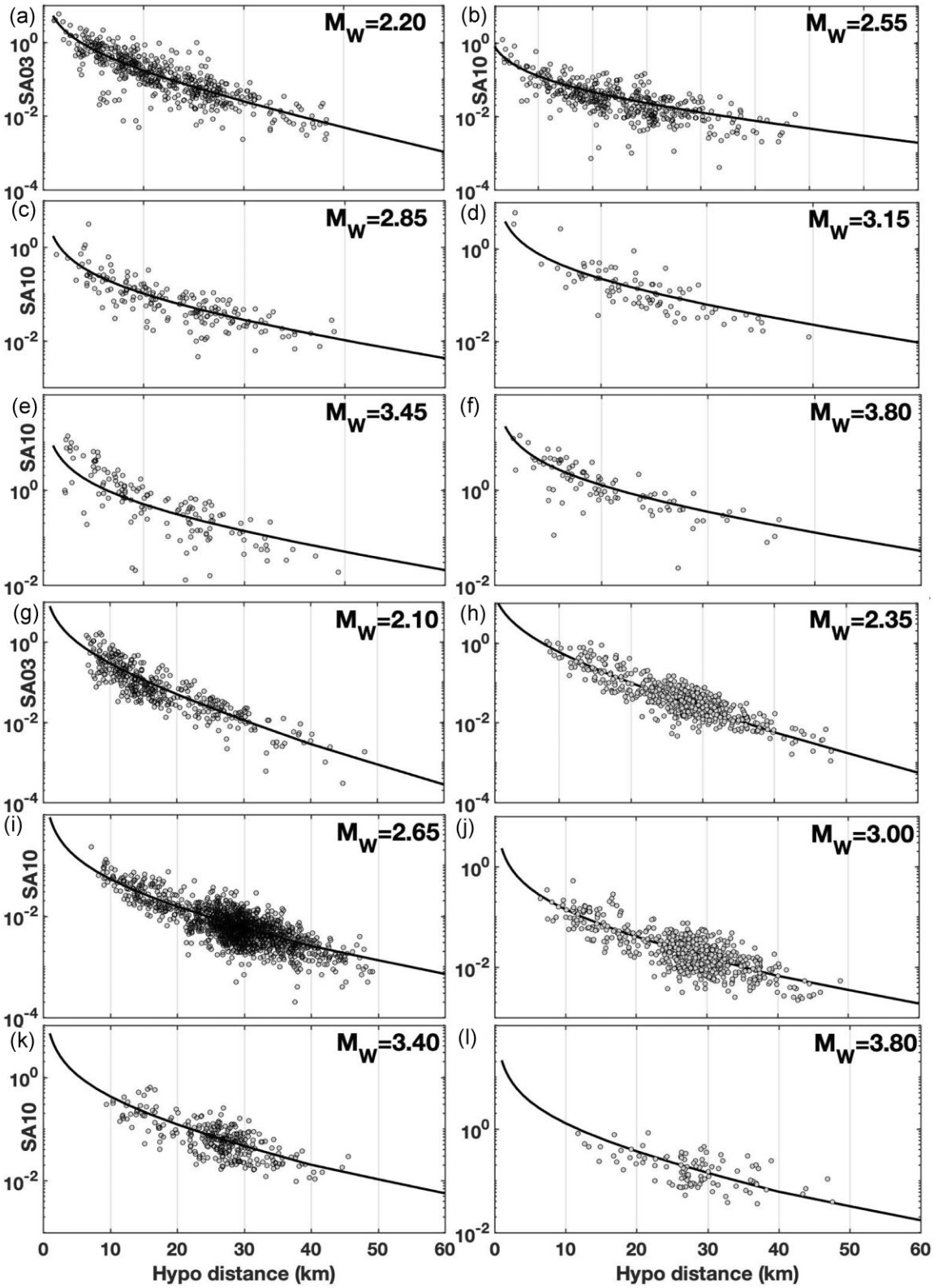

Figure 9. Comparison of the SA data used during the calibration process with the final M_W(SA) relations (black lines) tuned for the (a)–(f) shallow events and (g)–(l) deep events. The reference value M_W is reported in each panel.

Using the equations for M_W(SA), we estimate SA values for comparison with the stochastic simulations for $0.0 \leq M_W \leq 4.0$ (Fig. 6). In the shallow case (Fig. 6a), SA03 derived from the empirical equations overestimate the synthetic values for $M_W = 4$, which are influenced by the saturation effects, but agree with the simulations for $M_W = 2.0$ and 3.0; minor differences may possibly be related to the unmodelled source or site effects (Atkinson *et al.* 2014); SA10 (Fig. 6c) are consistent with simulations for $M_W \geq 2.0$, as were

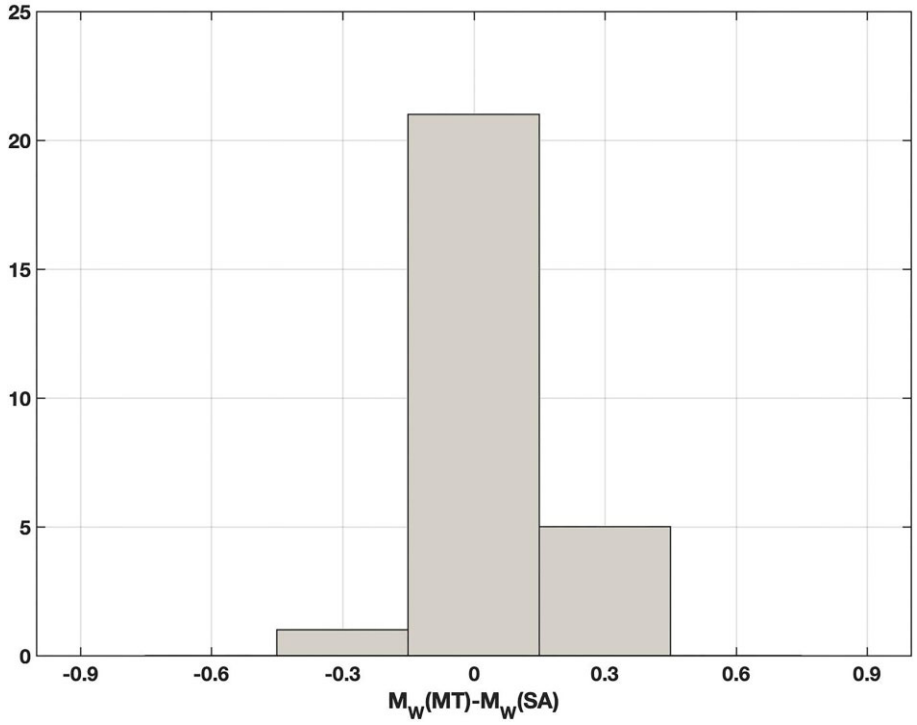

Figure 10. Differences between M_W(MT) and M_W(SA) versus event number.

both SA03 (Fig. 6b) and SA10 (Fig. 6d) calculated for deep events. Fig. 6 also shows that the empirical relationships overestimate the simulations for $M_W = 1.0$ and 0.0, and therefore they cannot be applied to $M_W < 2.0$ events.

For 22 events in the magnitude range $3.0 \leq M_W \leq 4.0$ examined in this study, we can compare the values estimated from the M_W(SA) relations and the M_W(MT) moment tensor. Fig. 10 shows that the differences in magnitude estimates, within the associated uncertainties are negligible for almost all events considered.

4 M_L–M_W RELATIONSHIPS

In the final step of our study, we correlated the M_W values obtained in this study with the corresponding M_L values reported in the Etnean seismicity catalogue (Alparone *et al.* 2015a, 2020a,b, 2022; Barberi *et al.* 2020); for M_L we consider an error of ± 0.27, as estimated by Tuvè *et al.* (2015).

First, we correlate the M_W determined from the moment tensors with M_L (Fig. 11a):

$$M_W\,(MT) = 1.01\,(\pm 0.01)\,M_L - 0.02\,(\pm 0.02) \quad \text{for } 3.4 \leq M_L \leq 4.8 \qquad (7)$$

Then we obtain the relationship M_W–M_L for the $M_{W\,SA}$ obtained from eqs (5a) and (5b), (6a) and (6b) (Figs 11b and c):

$$M_W\,(SA) = 0.96\,(\pm 0.01)\,M_L + 0.17\,(\pm 0.03) \quad \text{for } 2.0 \leq M_W < 4.0 \qquad (8a)$$

$$M_W\,(SA) = 1.03\,(\pm 0.01)\,M_L - 0.01\,(\pm 0.02) \quad \text{for } 2.0 \leq M_W < 4.0 \qquad (8b)$$

Since M_W and M_L can be considered equivalent for both the moment tensor and M_W (SA) in shallow and deep cases (Fig. 10), and to cover as wide an interval of magnitudes as possible, we have combined all M_W values obtained in this study. Fig. 6 shows that relations (4) and (5) are not suitable for estimating M_W for magnitude $M_L < 2.0$ because they overestimate the values of SA in this magnitude range. Therefore, to extend our relation to $M_L = 1.0$, we considered the M_W calculated from the spectral analysis of *P* waves in the range $1.0 \leq M_L < 2.0$. Finally, we obtained a data set of 633 M_W values (Fig. 11d). The relationship between M_W and M_L is as follows:

$$M_W = 0.97\,(\pm 0.01)\,M_L + 0.15\,(\pm 0.01) \quad \text{for } 1.0 \leq M_L \leq 4.8 \qquad (9)$$

5 DISCUSSION AND CONCLUSIONS

Estimating the magnitude and energy released by earthquakes in volcanic environments is one of the most important issues in the study of volcanic seismicity to understand the generation mechanism and predict the likely evolution of volcanic activity. Indeed, the cumulative seismic moment of VT can be used to estimate the volume of intruded magma and thus the probability of impending eruption and the seismic moments are often derived from M_W (Meyer *et al.* (2021). In addition, rapid and robust M_W estimates are highly desirable in high-risk volcanic regions and near densely populated areas because they have important implications for seismic hazard assessment. The importance of estimating M_W even for small events is shown by Petrosino *et al.* (2008), who observed that in the Campi Flegrei volcanic region, the absolute errors in M_W for earthquakes recorded with a low SNR are lower than the errors of M_L.

M_W estimates from moment tensor inversions of broad-band waveforms are considered the most robust solutions (e.g. Gasperini *et al.* 2012). However, in order to be used for seismic hazard assessment, and to cover the widest possible magnitude range including the low magnitude values typical of Etna seismicity, in this study we considered independent methods for calculating robust M_W of seismic events recorded in 2005–2020 time window. Our goal is to provide independent M_W estimates and empirical relationships specifically calibrated for the Etna region. To achieve our goal we compiled a data set with complete seismic moment tensors for 71 events of magnitude $3.4 \leq M_L \leq 4.8$. The obtained solutions

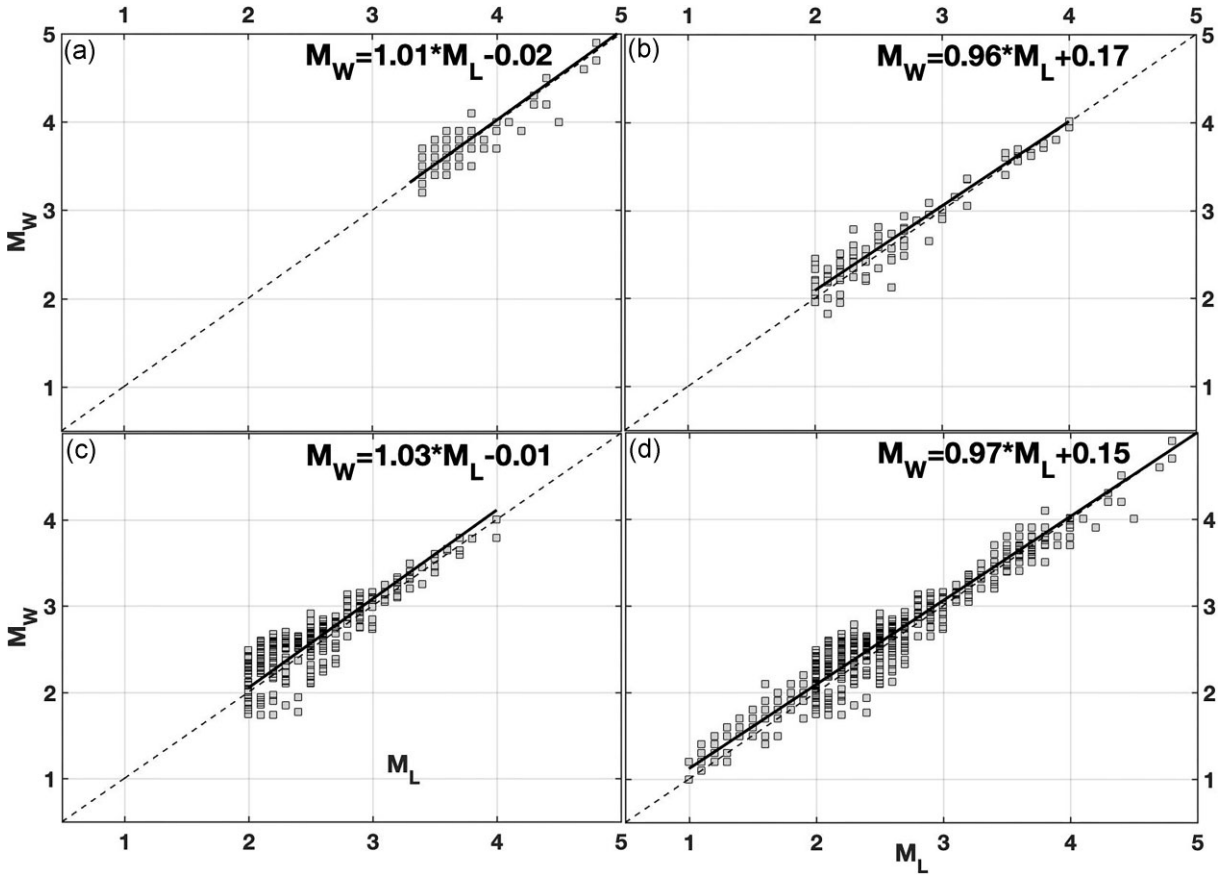

Figure 11. Orthogonal regressions between M_L versus M_W for the Etna earthquakes considered in this study (squares); M_W values are computed by (a) complete moment tensor, (b) SA for shallow and (c) deep events and (d) merging all M_W estimated in this study.

show that during the study period, the DC component dominated the source mechanisms. In contrast, mechanisms unrelated to DC were predominantly observed in the PFS (Fig. 5b), likely due to the presence of fluid circulation. The association between non-double-couple earthquakes and fluids is complex and multifaceted, involving a variety of physical processes (e.g. Julian *et al.* 1998). For instance, the flow of fluids can create pressure imbalances and lead to development or closure of cracks or fractures in rocks, increase pore pressure and reduce friction between rocks.

To enrich the M_W data set for the smallest earthquakes, we calibrated an independent data-driven equation for M_W as a function of SA, for shallow and deep events of Etna seismicity in the magnitude range $2.0 \leq M_W < 4.0$ (eqs 5a, 5b, 6a, 6b). Comparison of the values of M_W(SA) and M_W obtained from the moment tensor for the same events in this study demonstrates the robustness of our results and the compatibility of the two solution data sets. On this basis, we combined the independent data sets obtained in this study to obtain a fine-tuned empirical M_W–M_L relationship for the Etna region in the range $1.0 \leq M_L \leq 4.8$ (eq. 9). The new relationship is fully comparable to the preliminary relationship M_W–M_L of Saraò *et al.* (2016).

For the seismicity studied the M_L and M_W scale almost as 1:1 within the associated errors. Several studies (Hanks & Boore 1984; Edwards *et al.* 2010; Munafò *et al.* 2016; Dost *et al.* 2018; Moratto *et al.* 2017, 2019; Lanzoni *et al.* 2020) have demonstrated that the difference between M_L and M_W tends to increase for small to micro events due to source and rupture complexity, radiation pattern and rupture directivity, stress drop, wave propagation and seismometer response (Deichmann 2006). The value at which the ratio of the magnitudes M_L and M_W changes varies for different data sets and geological settings, and it decreases when the global absorption factor is small, such as when sensors are very close to hypocentres, as in deep mines or on volcanoes (Deichmann 2017). For these reasons, we recommend that users apply the data-driven relationships that we provide in this study within the magnitude ranges in which they were calibrated.

The relation between M_L and M_W is crucial for seismic hazard since it affects Gutenberg–Richter parameters and completeness (Lanzoni *et al.* 2020) and it can lead to possible biases in the probability of occurrence of large earthquakes (Staudenmaier *et al.* 2018). Our study is therefore a fundamental building block for accurate seismic hazard assessment and studies on the dynamics of the Etna volcano.

ACKNOWLEDGMENTS

We thank the editor Huajian Yao, Domenico Di Giacomo and an anonymous reviewer for their constructive suggestions and efforts to improve our paper. We acknowledge the INGV-OE seismic technical staff for the maintenance of the seismic monitoring network. This work was supported by Project V3—Multidisciplinary analysis of the relationships between tectonic structures and volcanic activity (Etna, Vulcano-Lipari system)—agreement INGV-DPC 2012-2021; WP2–task 8 'Caratterizzazione di sorgenti sismiche in near real-time: applicazione al monitoraggio delle aree vulcaniche siciliane' in the frame of B2 DPC-INGV 2019-2021 project; IMPACT

Department strategic project (WP2_Task 3); 'Project PE0000005–RETURN funded under the National Recovery and Resilience Plan (NRRP), Mission 4 Component 2 Investment 1.3–Call for tender no. 341 of 2022 March 15 of Italian Ministry of University and Research funded by the European Union—NextGenerationEU.

DATA AVAILABILITY

Data set of moment tensor solutions Saraò *et al.* (2016) and Cocina *et al.* (2022). Seismic waveforms of the seismic events investigated in this study can be downloaded from EIDA Italia (http://eida.ingv.it/).

CONFLICT OF INTEREST

The authors declare that the research was conducted in the absence of any commercial or financial relationships that could be construed as a potential conflict of interest.

AUTHORS CONTRIBUTION

Angela Saraò: Conceptualization, Validation, Formal analysis, Investigation, Original Draft writing, Supervision, Funding acquisition: **Luca Moratto and Elisabetta Giampiccolo**: Formal analysis, Investigation, Visualization, Original Draft writing; **Ornella Cocina**: Resources, Data Curation, Visualization, Project administration, Funding acquisition. All the authors contributed to the Writing—Review & Editing.

REFERENCES

Abercrombie, R.E., 2015. Investigating uncertainties in empirical Green's function analysis of earthquake source parameters, *J. geophys. Res. Solid Earth,* **120,** 4263–4277.

Alparone, S. C. *et al.*, 2020c. *Mt. Etna Seismic Catalog 2014-2016 (Version 1) [Data set]*. Istituto Nazionale di Geofisica e Vulcanologia (INGV).

Alparone, S., Barberi, G., Cocina, O., Giampiccolo, E., Musumeci, C. & Patanè, D., 2012. Intrusive mechanism of the 2008-2009 Mt. Etna eruption: constraints by tomographic images and stress tensor analysis, *J. Volc. Geotherm. Res.,* **229-230,** 50–63.

Alparone, S.C. *et al.*, 2015. *Mt. Etna Seismic Catalog 2000-2010 [Data set]*. Istituto Nazionale di Geofisica e Vulcanologia (INGV)—Osservatorio Etneo.

Alparone, S.C. *et al.*, 2020a. *Mt. Etna Revised and Concise Seismic Catalog from 1999 (EtnaRCSC) [Data set]*. Istituto Nazionale di Geofisica e Vulcanologia (INGV).

Alparone, S.C. *et al.*, 2020b. *Mt. Etna Seismic Catalog 2011-2013 [Data set]*. Istituto Nazionale di Geofisica e Vulcanologia (INGV).

Alparone, S.C. *et al.*, 2022. *Mt. Etna Seismic Catalog 2017-2019 (Version 1) [Data set]*. Istituto Nazionale di Geofisica e Vulcanologia (INGV).

Andrews, D.J., 1986. Objective determination of source parameters and similarity of earthquakes of different sizes, in Earthquake source mechanics, Das, S., Boatwright, J. & Scholz, C.H., (eds), *Am. Geophys. Union, Geophys. Monogr. Ser.,* vol. **6,** pp. 259–267.

Atkinson, G., Wesley Greig, D. & Yenier, E., 2014. Estimation of moment magnitude (M) for small events (M<4) on local networks, *Seismol. Res. Lett.,* **85,** 1116–1124.

Azzaro, R., Bonforte, A., D'Amico, S., Guglielmino, F. & Scarfì, L., 2020. Stick-slip vs. stable sliding fault behaviour: A case-study using a multidisciplinary approach in the volcanic region of Mt. Etna (Italy), *Tectonophysics,* **790,** 228554, doi:10.1016/j.tecto.2020.228554.

Azzaro, R. & D'Amico, S., 2019. *Catalogo Macrosismico dei Terremoti Etnei (CMTE)*. Istituto Nazionale di Geofisica e Vulcanologia (INGV).

Azzaro, R., D'Amico, S., Peruzza, L. & Tuvè, T., 2012. Earthquakes and faults at Mt. Etna: problems and perspectives for a time-dependent probabilistic seismic hazard assessment in a volcanic region, *Boll. Geof. Teor. Appl.,* **53,** 75–88.

Azzaro, R., D'Amico, S. & Tuvè, T., 2015. Seismic hazard assessment in the volcanic region of Mt. Etna (Italy): a probabilistic approach by macroseismic data applied to volcano-tectonic seismicity, *Bull. Earthq. Eng.,* **14,** 1813–1825.

Barberi, G. *et al.*, 2020. *Mt. Etna Revised Seismic Catalog from 2020 (EtnaRSC2020) (Version 1) [Data set]*. Istituto Nazionale di Geofisica e Vulcanologia (INGV).

Bianco, F., Castellano, M., Del Pezzo, E. & Ibanez, J.M., 1999. Attenuation of short-period seismic waves at Mt Vesuvius, Italy, *Geophys. J. Int.,* **138,** 67–76.

Bonaccorso, A. & Giampiccolo, E., 2020. Balance between deformation and seismic energy release: the Dec 2018 'double-dike' Intrusion at Mt. Etna, *Front. Earth Sci.,* **8,** 583815, doi:10.3389/feart.2020.583815.

Boore, D., 1983. Stochastic simulation of high-frequency ground motion based on seismological models of the radiated spectra, *Bull. seism. Soc. Am.,* **73,** 1865–1894.

Boore, D., 2003. Simulation of ground motion using the stochastic method, *Pure appl. Geophys.,* **160,** 635–676.

Bormann, P. & Di Giacomo, D., 2015. Earthquake: magnitudes, energy, and moment, in: Meyers, R.(eds) *Encyclopedia of Complexity and Systems Science*. Springer, Berlin, Heidelberg.

Brune, J., 1970. Tectonic stress and the spectra of seismic shear waves from earthquakes, *J. geophys. Res.,* **75,** 4997–5009.

Castellaro, S., Mulargia, F. & Kagan, Y.Y., 2006. Regression problems for magnitudes, *Geophys. J. Int.,* **165,** 913–930.

Centamore, C., Montalto, A. & Patanè, G., 1997. Self-similarity and scaling relations for microearthquakes at Mt. Etna volcano (Italy), *Phys. Earth planet. Inter.,* **103,** 165–177.

Cocina, O., Saraò, A., Cannata, A. & Montalto, P.M., 2022. *Full Moment Tensor Solutions for $M_L \geq 3.5$ Etna Earthquakes from October 2018 to December 2020 (CMTC_2018-2020) (Version 1) [Data set]*. Istituto Nazionale di Geofisica e Vulcanologia (INGV).

Cocina, O., Saraò, A., Scognamiglio, L., Cannata, A. & Montalto, P., 2020. A feasibility study on the near real-time calculation of the complete seismic moment tensor of the Etna Seismicity: application to the earthquakes occurred during the December 2018 eruption. 4 Conferenza Rittmann, Catania 12-14 February 2020, *Misc. INGV,* **52,** 99, ISSN 2039-6651.

D'Amico, S., Meroni, F., Sousa, M.L. & Zonno, G., 2016. Building vulnerability and seismic risk analysis in the urban area of Mt. Etna volcano (Italy), *Bull. Earthq. Eng.,* **14,** 2031–2045.

De Gori, P., Chiarabba, C., Giampiccolo, E., Martinez–Arèvalo, C. & Patanè, D., 2011. Body wave attenuation heralds incoming eruptions at Mount Etna, *Geology,* **39,** 503–506.

De Gori, P., Chiarabba, C. & Patanè, D., 2005. Qp structure of Mount Etna: constraints for the physics of the plumbing system, *J. geophys. Res.,* **110,** B05303, doi:10.1029/2003JB002875.

De Lorenzo, S., Giampiccolo, E., Martinez-Arevalo, C., Patanè, D. & Romeo, A., 2010. Fault plane orientations of microearthquakes at Mt. Etna from the inversion of P-wave rise times, *J. Volc. Geotherm. Res.,* **189,** 247–256.

Deichmann, N., 2006. Local magnitude, a moment revisited, *Bull. seism. Soc. Am.,* **96,** 1267–1277.

Deichmann, N., 2017. Theoretical basis for the observed break in M_L /M_W scaling between small and large earthquakes, *Bull. seism. Soc. Am.,* **107,** 505–520.

Del Pezzo, E. & Petrosino, S., 2001. A local-magnitude scale for Mt. Vesuvius from synthetic Wood-Anderson seismograms, *J. Seismol.,* **5,** 207–215.

Díaz-Moreno, A. *et al.*, 2018. New insights on Mt. Etna's crust and relationship with the regional tectonic framework from joint active and passive P-wave seismic tomography, *Surv. Geophys.,* **39,** 57–97.

Dost, B., Edwards, B. & Bommer, J., 2018. The relationship between M and M_L: a review and application to induced seismicity in the Groningen Gas Field, The Netherlands, *Seism. Res. Lett.,* **89,** 1062–1064.

Dreger, D. & Helmberger, D.V., 1993. Determination of source parameters at regional distances withthree-componentt sparse network data, *J. geophys. Res.,* **98,** 8107–8125.

Dreger, D., Uhrhammer, R., Pasyanos, M., Franck, J. & Romanowicz, B., 1998, Regional and far-Regional earthquake locations and source parameters using sparse broadband networks: a test on the ridgecrest sequence, *Bull. seism. Soc. Am.,* **88,** 1353–1362.

Dreger, D.S., 2003. TDMT_INV: time-domain seismic moment tensor inversion, In: Lee, W.H.K., Kanamori, H., Jennings, P.C. & Kisslinger, C.(eds.), *International Handbook of Earthquake and Engineering Seismology,* vol. **81 B,** p. 1627, Academic Press, Amsterdam.

Eberhart-Phillips, D. & Chadwick, M., 2002. Three-dimensional attenuation model of the shallow Hikurangi subduction zone in the Raukumara Peninsula, New Zealand, *J. geophys. Res.,* **107**(B2), doi:10.1029/2000JB000046.

Edwards, B. & Douglas, J., 2014. Magnitude scaling of induced earthquakes, *Geothermics,* **52,** 132–139.

Edwards, B.B., Allmann Fah, D. & Clinton, J., 2010. Automatic computation of moment magnitudes for small earthquakes and the scaling of local to moment magnitude, *Geophys. J. Int.,* **183,** 407–420.

Eulenfeld, T., Dahm, T., Heimann, S. & Wegler, U., 2021. Fast and robust earthquake source spectra and moment magnitudes from envelope inversion, *Bull. seism. Soc. Am.,* **112,** 878–893.

Gasperini, P., Lolli, B., Vannucci, G. & Boschi, E., 2012. A comparison of moment magnitude estimates for the European-Mediterranean and Italian regions, *Geophys. J. Int.,* **190,** 1733–1745.

Giampiccolo, E., D'Amico, S., Patanè, D. & Gresta, S., 2007. Attenuation and source parameters of shallow microearthquakes at Mt. Etna Volcano, Italy, *Bull. seism. Soc. Am.,* **97,** 184–197.

Guardato, S., Donnarumma, G.P., Riccio, R., Del Pezzo, E. & Iannaccone, G., 2022. Moment magnitude (M_W) from hydrophone records of low energy volcanic quakes, *J. Seismol.,* **26,** 875–882.

Hanks, T.C. & Boore, D.M., 1984. Moment-magnitude relations in theory and practice, *J. geophys. Res.,* **89,** 2033–2046.

Hanks, T.C. & Kanamori, H., 1979. A moment magnitude scale, *J. geophys. Res.,* **84,** 2348–2350.

Havskov, J.J., Pena, A., Ibanez, J.M., Ottemoller, L. & Martinez-Arevalo, C., 2003. Magnitude scales for very local earthquakes. Application for Deception Island Volcano (Antarctica), *J. Volc. Geotherm. Res.,* **128,** 115–133.

Julian, B.R., Miller, A.D. & Foulger, G.R., 1998. Non-double-couple earthquakes 1. Theory, *Rev. Geophys.,* **36,** 525–549.

Kanamori, H., 1983. Magnitude scale and quantification of earthquakes, *Tectonophysics,* **93,** 185–199.

Kanamori, H., Mori, J., Hauksson, E., Heaton, T., Hutton, K. & Jones, L., 1993. Determination of earthquakes energy release and M_L using TERRAscope, *Bull. seism. Soc. Am.,* **83,** 330–346.

Keilis Borok, V. I., 1959. On estimation of the displacement in an earthquake source dimension, *Ann. Geofis.,* **12,** 205–214.

Langer, H., Tusa, G., Scarfì, L. & Azzaro, R., 2016. Ground-motion scenarios on Mt. Etna inferred from empirical relations and synthetic simulations, *Bull. Earthq. Eng.,* **14,** 1917–1943.

Lanzoni, A., Moratto, L., Priolo, E. & Romano, M.A., 2020. Fast M_W estimation of microearthquakes recorded around the underground gas storage in the Montello-Collalto area (Southeastern Alps, Italy), *J. Seismol.,* **24,** 1029–1043.

Madariaga, R. 1976. Dynamics of an expanding circular fault, *Bull. seism. Soc. Am.,* **66,** 639–666.

Martínez-Arevalo, C., Patane, D., Rietbrock, A. & Ibáñez, J.M., 2005. The intrusive process leading to the Mt. Etna 2001 flank eruption: constraints from 3D attenuation tomography, *Geophys. Res. Lett.,* **32,** L21309, doi:10.1029/2005GL023736.

Meyer, K., Biggs, J. & Aspinall, W., 2021. A Bayesian reassessment of the relationship between seismic moment and magmatic intrusion volume during volcanic unrest, *J. Volc. Geother. Res.,* **419,** 107375, doi:10.1016/j.jvolgeores.2021.107375.

Minson, S. & Dreger, D., 2008. Stable inversions for complete moment tensors, *Geophys. J. Int.,* **174,** 585–592.

Moratto, L., Romano, M.A., Laurenzano, G., Colombelli, S., Priolo, E., Zollo, A., Saraò, A. & Picozzi, M., 2019. Source parameter analysis of microearthquakes recorded around the underground gas storage in the Montello-Collalto Area (Southeastern Alps, Italy), *Tectonophysics,* **762,** 159–168.

Moratto, L., Saraò, A. & Priolo, E., 2017. Moment magnitude (M_W) estimation of weak seismicity in northeastern Italy, *Seism. Res. Lett.,* **88,** 1455–1464.

Munafò, I., Malagnini, L. & Chiaraluce, L., 2016. On the relations between M_W and M_L for small earthquakes, *Bull. seism. Soc. Am.,* **106,** 2402–2408.

Ottemöller, L. & Havskov, J., 2003. Moment magnitude determination for local and regional earthquakes based on source spectra, *Bull. seism. Soc. Am.,* **93,** 203–214.

Panza, G.F. & Saraò, A., 2000. Monitoring volcanic and geothermal areas by full seismic moment tensor inversion: are non-double couple components always artefacts of modelling?, *Geophys. J. Int.,* **143,** 353–364.

Patanè, D., Cocina, O., Falsaperla, S., Privitera, E. & Spampinato, S., 2004. Mt. Etna volcano: a seismological frame work, in *The Mt. Etna Volcano,* in Mt. Etna: Volcano Laboratory, pp. 147–165. eds A. Bonaccorso, S. Calvari, M. Coltelli, C. Del Negro and S. Falsaperla, AGU, Washington, D.C.

Patanè, D., Ferrucci, F., Giampiccolo, E. & Scaramuzzino, L., 1997. Source scaling of microearthquakes at Mt. Etna volcano and in the Calabrian Arc (southern Italy), *Geophys. Res. Lett.,* **24,** 1879–1882.

Patanè, D., Ferrucci, F. & Gresta, S., 1994. Spectral features of microearthquakes in volcanic areas: attenuation in the crust and amplitude response of the site at Mt. Etna, Italy, *Bull. seism. Soc. Am.,* **84,** 1842–1860.

Patanè, D. & Giampiccolo, E., 2004. in Faulting processes and earthquake source parameters at Mt. Etna: state of the art and perspectives, *American Geophysical Monograph,* vol. **143,** pp. 167–189, eds Bonaccorso, A., Calvari, S., Coltelli, M., Del Negro, C. & Falsaperla, S., Mt. Etna: Volcano Laboratory.

Patanè, G., Coco, G., Corrao, M., Imposa, S. & Montalto, A., 1995. Source parameters of seismic events at Mount Etna volcano, Italy, during the outburst of the 1991-1993 eruption, *Phys. Earth planet. Inter.,* **89,** 149–162.

Petrosino, S., De Siena, L. & Del Pezzo, E., 2008. Recalibration of the magnitude scales at Campi Flegrei, Italy, on the basis of measured path and site and transfer functions, *Bull. seism. Soc. Am.,* **98,** 1964–1974.

Pondrelli, S., 2002. European-Mediterranean Regional centroid-moment tensors catalog (RCMT) [Data set]. Istituto Nazionale di Geofisica e Vulcanologia (INGV), *Bull. seism. Soc. Am.,* **98,** 1964–194, https://doi.org/10.13127/rcmt/euromed.

Richter, C. F., 1935. An instrumental earthquake magnitude scale, *Bull. seism. Soc. Am.,* **25,** 1–32.

Rösler, B. & Stein, S., 2022. Consistency of non-double-couple components of seismic moment tensors with earthquake magnitude and mechanism, *Seism. Res. Lett.,* **93,** 1510–1523.

Rovida, A., Locati, M., Camassi, R., Lolli, B. & Gasperini, P., 2020. The Italian earthquake catalogue CPTI15, *Bull. Earthq. Eng.,* **18,** 2953–2984.

Rovida, A., Locati, M., Camassi, R., Lolli, B., Gasperini, P. & Antonucci, A., 2022. *Catalogo Parametrico dei Terremoti Italiani (CPTI15), Versione 4.0*. Istituto Nazionale di Geofisica e Vulcanologia (INGV).

Saikia, C.K., 1994. Modified frequency-wavenumber algorithm for regional seismograms using Filon's Quadrature-modeling of lg waves in eastern North America, *Geophys. J. Int.,* **118,** 142–158.

Saraò, A., Cocina, O., Moratto, L. & Scarfì, L., 2016. Dynamics and kinematics of the eastern flank from seismological and ground deformation analyses (Etna). Earthquake features through the seismic moment tensor, In Miscellanea INGV (Vol. **29,** pp. 1–172). INGV Istituto Nazionale di Geofisica e Vulcanologia.

Saraò, A., Cocina, O., Privitera, E. & Panza, G.F., 2010. The dynamics of the 2001 Etna eruption as seen by full moment tensor analysis, *Geophys. J. Int.,* **181,** 951–965.

Saraò, A., Panza, G.F., Privitera, E. & Cocina, O., 2001. Non-double-couple mechanisms in the seismicity preceding the 1991–1993 Etna volcano eruption, *Geophys. J. Int.,* **145,** 319–335.

Saraò, A., Sugan, M., Bressan, G., Renner, G. & Restivo, A., 2021. A focal mechanism catalogue of earthquakes that occurred in the southeastern Alps and surrounding areas from 1928–2019, *Earth Syst. Sci. Data,* **13,** 2245–2258.

Scherbaum, F., 1990. Combined inversion for the three-dimensional Q structure and source parameters using microearthquake spectra, *J. geophys. Res.,* **95**(12), 12, 423–12, 438.

Scognamiglio, L., Tinti, E. & Quintiliani, M., 2006. Time domain moment tensor (TDMT) [Data set]. Istituto Nazionale di Geofisica e Vulcanologia (INGV), doi:10.13127/tdmt.

Siniscalchi, A. *et al.*, 2010. Insights into fluid circulation across the Pernicana Fault (Mt. Etna, Italy) and implications for flank instability, *J. Volc. Geotherm. Res.,* **193,** 137–142.

Staudenmaier, N., Tormann, T., Edwards, B., Deichmann, N. & Wiemer, S., 2018. Bilinearity in the Gutenberg-Richter relation based on M_L for magnitudes above and below 2, from systematic magnitude assessments in Parkfield (California), *Geophys. Res. Lett.,* **45,** 6887–6897.

Tuvè, T., D'Amico, S. & Giampiccolo, E., 2015. A new MD-ML relationship for Mt. Etna earthquakes (Italy), *Ann. Geophys.,* **58**(6), S0657, doi:10.4401/ag-6830.

Villani, F. *et al.*, 2020. Surface ruptures database related to the 26 December 2018, M_W 4.9 Mt. Etna earthquake, southern Italy, *Sci. Data,* **7,** 42, doi:10.1038/s41597-020-0383-0.

Zúñiga, F.R., Wyss, M. & Scherbaum, F., 1988. A moment-magnitude relation for Hawaii, *Bull. seism. Soc. Am.,* **78,** 370–373.

SUPPORTING INFORMATION

Supplementary data are available at *GJI* online.

Table S1: Locations and Source parameters of the earthquakes selected for the analysis (see the main text). The radius, $r = 0.32 * v/f_c$, was calculated following Madariaga (1976). Stress drop $\Delta\sigma = 7M_0/16r^3$ was estimated using the average values of M_0 and r (Keilis-borok 1959). M_W was estimated from M_0 following Hanks & Kanamori (1979) relationship.

Table S2: Earthquakes locations, local magnitude (M_L), seismic moment (M_0) and moment magnitude used for calibration ($M_{W(CAL)}$) at shallow depths ($h \leq 5$ km)

Table S3: Earthquakes locations, local magnitude (M_L), seismic moment (M_0) and moment magnitude used for calibration ($M_{W(CAL)}$) below 5 km of depth.

Please note: Oxford University Press is not responsible for the content or functionality of any supporting materials supplied by the authors. Any queries (other than missing material) should be directed to the corresponding author for the paper.